

# **Ion Trapping**

Notes and Simulations

February 4, 2026

Wanxiang Zhang

# Personal Note

This is a rather short summary of the ideas, calculations and experiments conducted in the literature (listed in the references at the end) regarding ion trapping for quantum computation, as well as some simple simulations conducted using Comsol Multiphysics to validate the key insights. Thus, it can be treated as a literature overview and not much original. The author will be thankful for any technical or spelling error spotted.

I am grateful for Prof. Yiheng Lin and Dr. Yue Li for guidance. Also special thanks for the good campus environment at USTC and the funded FuSep program for this summer research opportunity.

## Contents

<b>1</b>	<b>Ion Traps</b>	<b>2</b>
1.1	Linear Paul Trap [1]	2
1.2	Surface Trap Designs	3
1.3	Penning Trap	5
<b>2</b>	<b>Quantum Mechanics of Ions</b>	<b>7</b>
2.1	Motional and Internal States	7
2.2	Interaction and Coupling with Fields	8
2.3	Rabi Oscillation	9
2.4	Open Quantum Systems	10
2.5	Stimulated Raman Transitions	10
2.6	Initialisation (Cooling Techniques)	12
2.7	Quantum Logic Gates	13
2.8	Detection of Internal States	16
<b>3</b>	<b>Dynamical Decoupling (MW) [2]</b>	<b>16</b>
3.1	Theory	16
3.2	Experimental Design and Demonstration	17
3.3	Magnetic Field Modeling	18
3.4	Alternative Design	20
<b>4</b>	<b>Relevant Sources</b>	<b>22</b>

# 1 Ion Traps

## 1.1 Linear Paul Trap [1]

By Laplace's equation for electric potential in a vacuum (no net charge density):

$$\nabla^2 V = 0 \quad (1)$$

Hence it is impossible to have a naive quadratic potential with positive prefactors in both  $x$  and  $y$  directions, leading to instability (unbounded motion) in at least one direction. Instead, we must take consideration of either time-varying electric fields (Paul trap) or additional magnetic fields (Penning trap) for the purpose of confinement of ions.

A schematic design (electrodes) for a linear Paul-rf trap is shown here:

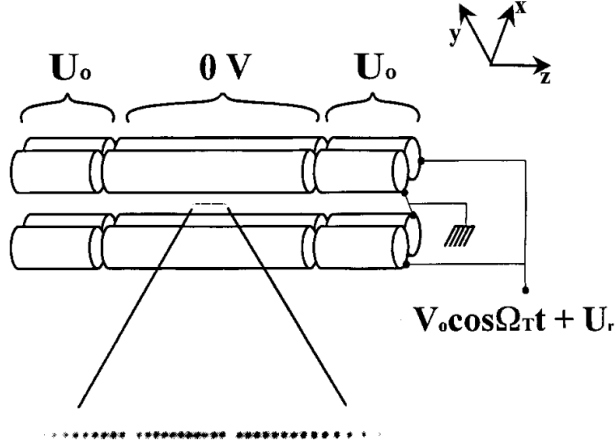


Figure 1: Linear Paul-rf Trap Design

Consider the time-varying potential created by the trap: (near the center and axis of the trap, quadratic approx.)

$$\phi_t = (V_0 \cos(\Omega_T t) + U_r) \left( 1 + \frac{x^2 - y^2}{R^2} \right)$$

As well as the static harmonic well:

$$\phi_s = \frac{m}{2q} w_z^2 \left( z^2 - \frac{1}{2}(x^2 + y^2) \right)$$

where  $w_z = \sqrt{\frac{2\kappa q U_0}{mz_0^2}}$ .

For an ion of charge  $q$ , its motion will be dictated by:

$$m\ddot{\mathbf{x}} = -q\nabla\phi = -q\nabla(\phi_s + \phi_t) \quad (2)$$

Then one can obtain the simultaneous equations in  $x$  and  $y$  respectively. Take the  $x$ -direction first:

$$\begin{aligned}\phi &= \phi_s + \phi_t = \frac{m}{2q} w_z^2 \left( z^2 - \frac{1}{2}(x^2 + y^2) \right) + (V_0 \cos(\Omega_T t) + U_r) \left( 1 + \frac{x^2 - y^2}{R^2} \right) \\ m \frac{d^2 x}{dt^2} &= -q \left( \frac{mw_z^2}{2q} (-x) + (V_0 \cos(\Omega_T t) + U_r) \frac{x}{R^2} \right) \\ \frac{d^2 x}{dt^2} &= - \left( \frac{q}{m} \left( \frac{U_r}{R^2} - \frac{\kappa U_0}{z_0^2} \right) + \frac{qV_0}{mR^2} \cos(\Omega_T t) \right) x\end{aligned}$$

Upon making a substitution of  $\zeta = \Omega_T t / 2$ , we obtain the Mathieu equation(s) (similarly for  $y$ ), which is a set of simultaneous second-order ordinary differential equations:

$$\frac{d^2 x}{d\zeta^2} + \left( \underbrace{\frac{4q}{m\Omega_T^2} \left( \frac{U_r}{R^2} - \frac{\kappa U_0}{z_0^2} \right)}_{a_x} + 2 \underbrace{\left( \frac{2qV_0}{\Omega_T^2 m R^2} \right) \cos(2\zeta)}_{q_x} \right) x = 0 \quad (3)$$

$$\frac{d^2 y}{d\zeta^2} + \left( \underbrace{-\frac{4q}{m\Omega_T^2} \left( \frac{U_r}{R^2} + \frac{\kappa U_0}{z_0^2} \right)}_{a_y} + 2 \underbrace{\left( -\frac{2qV_0}{\Omega_T^2 m R^2} \right) \cos(2\zeta)}_{q_y} \right) y = 0 \quad (4)$$

Upon suitable approximations  $a_i < q_i^2 \ll 1$  (where  $i = x, y$ ), the approximate solutions can be given as:

$$\begin{aligned}u_i(t) &= A_i (\cos(\omega_i t + \phi_i) [1 + \frac{q_i}{2} \cos(\Omega_T t) \\ &\quad + \frac{q_i^2}{32} \cos(2\Omega_T t)] + \frac{\beta_i q_i}{2} \sin(\omega_i t + \phi_i) \sin(\Omega_T t))\end{aligned} \quad (5)$$

where  $\omega_i = \beta_i \frac{\Omega_T}{2}$ ,  $\beta_i \simeq \left[ a_i + \frac{q_i^2}{2} \right]^{1/2}$ . Here it is noted that the  $\cos(\Omega_T)$  and  $\cos(2\Omega_T)$  terms represent the micromotion of ions (undesirable). Under the limit above, the ion behaves as if under a harmonic pseudopotential with frequency (in radial direction) given by:

$$\omega_r = \beta_i \Omega_T / 2 \simeq \frac{q_x \Omega_T}{2\sqrt{2}} \quad (6)$$

To produce a "string" of ions linearly along the  $z$  axis, it is preferable to have  $w_r \gg w_z$  to force ions to the axis of the trap.

Note here that  $w_r$  is the radial COM vibrational frequency and there are  $3L$  normal modes of motion in total (of which  $L$  are related to the axial motion).

Albeit the discussion above for quadrupole ion traps seems to be limited to the particular geometry of the '4-rod electrodes' design, the key insight of confinement is generalisable to the other geometries such as blade traps or surface traps.

## 1.2 Surface Trap Designs

In comparison to the traditional rod-based designs, surface traps have better scalability. A simple design is proposed<sup>[6]</sup> as in *Figure 2*.

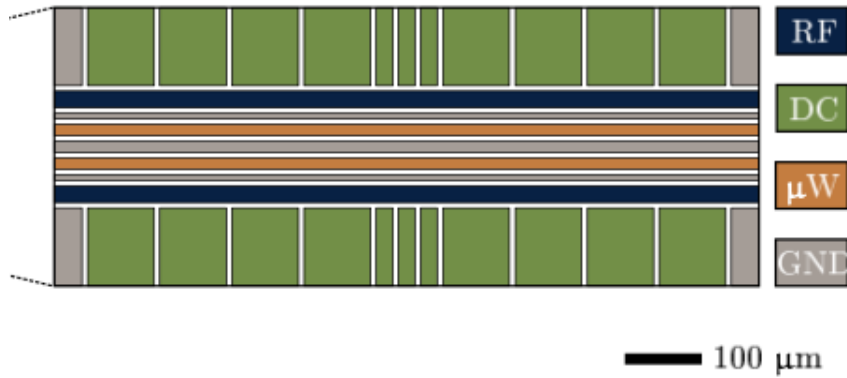


Figure 2: Surface Trap Design<sup>[6]</sup>

Here it is to be noted that the same mechanism of confinement works: DC and RF electrodes provide stationary and time-varying (periodic) electric fields which together set the stable (approximately) simple harmonic motion of the ion trapped just above the surface. The microwave ( $\mu W$ ) electrode is responsible for microwave-based control schemes (for individual addressing and logic gate operations).

To clearly see the validity of this model. We employ Comsol Multiphysics<sup>[7]</sup> for building and running the simulation of ion trajectories. Following the parameters discussed in literature<sup>[6]</sup>, the model is built with proper materials (gold for surface trap and air surrounded), as in *Figure 3*.

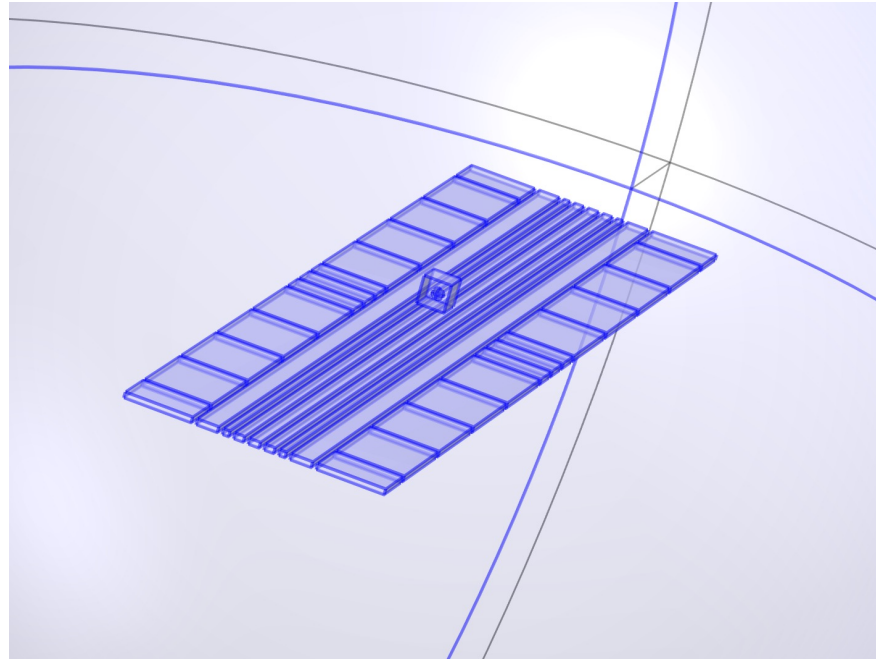


Figure 3: Comsol Model of a simple surface trap

Employing the built-in ACDC modules (using stationary, frequency-domain and time-dependent computation respectively), the particle trajectory resembles a periodic SHM motion with the amplitude of oscillation roughly between  $14\text{-}18\mu\text{m}$  with a secular motion angular frequency  $\omega \simeq 4.87 \cdot 10^7 \text{ rads}^{-1}$ , detail shown in *Figure 4*. The calculated pseudo-potential well depth is about  $0.04\text{eV}$ , relatively small compared to a typical rf-Paul trap (typically  $> 0.1\text{eV}$ ). But this is expected since we used a rather small RF & DC voltage (order of unity), and higher voltages could certainly create a larger potential depth.

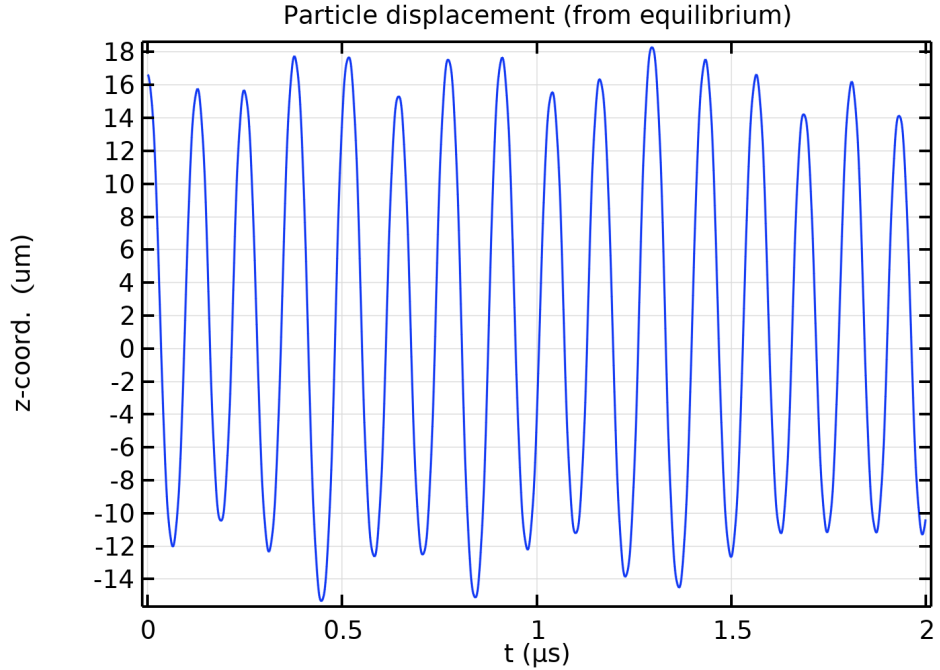


Figure 4: Oscillation of the trapped ion (normal direction to the plane of the surface trap)

### 1.3 Penning Trap

Alternative to the time-varying electric field scheme of a linear Paul trap, one can also consider the Penning trap, which uses purely static fields, with the compensating field being an additional magnetic field. The electromagnetic fields then constrain the affected ion to move in a predictable periodic way within the allowed range of confinement.

The designs of electrodes are similar to that of a 4-electrode Paul trap but with static fields. The additional insight is an extra axial ( $z$ -direction) magnetic field (hard to generate, though) which is strong enough to have a significant impact on ion motion dictated by the Lorentz force.

We start with the following static electric potential:

$$\Phi(x, y, z) = \frac{V_0}{2z_0^2} \left( z^2 - \frac{1}{2}(x^2 + y^2) \right)$$

Under the Lorentz force the EoM can be written as:

$$\begin{pmatrix} \dot{x} \\ \dot{y} \\ \dot{z} \end{pmatrix} = \underbrace{\frac{qB}{m}}_{\omega_c^2} \begin{pmatrix} y \\ -x \\ 0 \end{pmatrix} + \underbrace{\frac{qV_0}{mz_0^2}}_{\omega_z^2} \begin{pmatrix} x/2 \\ y/2 \\ -z \end{pmatrix}$$

where  $\omega_c$  is defined as the free cyclotron frequency and  $\omega_z$  as the axial frequency.

Without bothering to the trivial detail here, one can eventually obtain two frequencies of oscillations with the solution to a quadratic form:

$$\omega_{\pm} = \frac{1}{2} \left( \omega_c \pm \sqrt{\omega_c^2 - 2\omega_z^2} \right) \quad (7)$$

where  $\omega_+$  is the (faster) modified cyclotron frequency (but essentially very close to the free cyclotron frequency for  $\omega_z \ll \omega_c$ ), and  $\omega_-$  is the slower magnetron frequency.

For real stable solutions, one needs to fulfill the requirement that  $\omega_c^2 > 2\omega_z^2$ , which is equivalent to a condition on the magnitude of the magnetic flux density:

$$B > \sqrt{\frac{2mV_0}{qz_0^2}} \quad (8)$$

which is expected since in the opposite case the magnetic field is too small that the ion particle simply falls down the saddle-shaped static electric potential implying failure of confinement.

The two frequencies in (7) can be illustrated in a rough trajectory plotted as in *Figure 5*. The large circle is the result of motion under magnetron frequency while the fast local oscillations are due to (modified) cyclotron frequency.

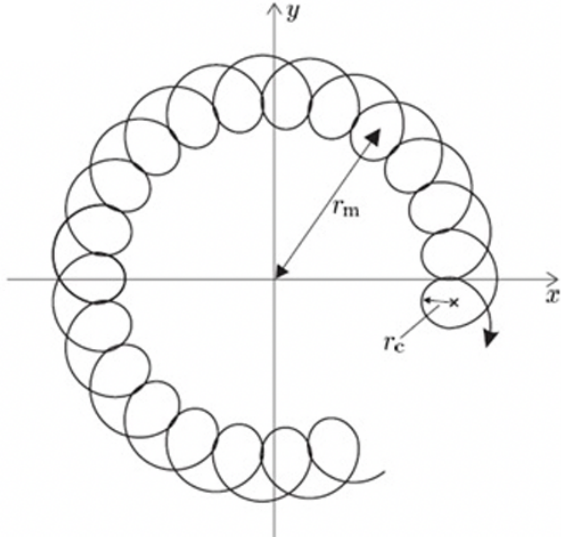


Figure 5: Ion Trajectory in Penning Traps [13]

## 2 Quantum Mechanics of Ions

### 2.1 Motional and Internal States

Following some ingenious experimental schemes to realise ion trapping, we return back to theories formulating the states of trapped ions. It is, to a good approximation for near-quadratic potentials, to describe the motion of a single trapped ion with the Hamiltonian of a standard quantum harmonic oscillator:

$$\hat{H}_{osc} = \hbar\omega_i \hat{n}_i \quad (9)$$

where  $\hat{n}_i = a_i^\dagger a_i$  and is the number operator, whilst  $a_i$  is the (lowering) ladder operator. Thus one can deduce the position operator  $\hat{z}$  (in  $z$  direction) by adding the lowering operator with the raising operator:

$$a + a^\dagger = \sqrt{\frac{m\omega}{2\hbar}} \left( \hat{z} + \frac{i}{mw} \hat{p} \right) + \sqrt{\frac{m\omega}{2\hbar}} \left( \hat{z} - \frac{i}{mw} \hat{p} \right) = \sqrt{\frac{2m\omega}{\hbar}} \hat{z}$$

Hence

$$\hat{z} = \underbrace{\sqrt{\frac{\hbar}{2m\omega}}}_{z_0} (a + a^\dagger) \quad (10)$$

$z_0 = \sqrt{\frac{\hbar}{2m\omega}}$  is the approximate spread of the zero-point wavefunction. For a typical  ${}^9Be^+$  ions in a trap where  $\omega_z/(2\pi) = 10$  MHz, we have  $z_0 = 7.5$  nm.

Thus it follows that the motional wavefunction (pure state assumed) of one mode can be written as a superposition of the SHO states:

$$\begin{aligned} \Psi_{motion} &= \sum_{n=0}^{\infty} c_n \exp\left(\frac{-iE_nt}{\hbar}\right) |n\rangle = \sum_{n=0}^{\infty} c_n \exp\left(\frac{-i(\hbar\omega_i n)t}{\hbar}\right) |n\rangle \\ &= \sum_{n=0}^{\infty} c_n \exp(-in\omega_i t) |n\rangle \end{aligned} \quad (11)$$

If we are only interested in the first two terms (for qubit applications), taking the simple form  $c_0 |0\rangle + c_1 \exp(-iw_1 t) |1\rangle$  is sufficient.

As with most spin-1/2 systems, it is appropriate to approximate a spin-1/2 magnetic moment under the influence of a (fictitious) magnetic field, to represent this "two-level" ion:

$$H_{internal} = -\boldsymbol{\mu} \cdot \mathbf{B} = -\mu_M S_z B_0 = \hbar\left(-\frac{\mu_M B_0}{\hbar}\right) S_z = \hbar\omega_0 S_z \quad (12)$$

Typically we expect the internal resonant frequency to be much larger than any motional mode frequency ( $\omega_0 \gg \omega_z$ ).

Given that there are two levels  $E_\uparrow = \hbar\omega_0/2$  and  $E_\downarrow = -\hbar\omega_0/2$ . We can write down the internal state wavefunction:

$$\begin{aligned} \Psi_{internal} &= C_\downarrow \exp(-iE_\downarrow t/\hbar) |\downarrow\rangle + C_\uparrow \exp(-iE_\uparrow t/\hbar) |\uparrow\rangle \\ &= C_\downarrow \exp(i\omega_0 t/2) |\downarrow\rangle + C_\uparrow \exp(-i\omega_0 t/2) |\uparrow\rangle \end{aligned} \quad (13)$$

In these experiments, measurement is performed using a laser beam that is carefully polarized and tuned to a specific atomic transition. This setup creates what's known as a "cycling" transition, where an atom in one internal state will scatter many photons while an atom in the other state scatters virtually none. By detecting even a modest number of these photons, we can achieve near-perfect (approaching 100%) discrimination efficiency between the two atomic states. Generally for  $n_d > 10$  (number of photons), detection will be highly efficient, with probability of error  $\sim 10^{-44}$ . The detail would be discussed again by the end of the chapter.

## 2.2 Interaction and Coupling with Fields

Consider the situations where fields resonantly drive transitions between internal or motional states and when they drive transitions between these states simultaneously (entanglement). Start with the interaction Hamiltonian: (magnetic coupling)

$$H_1 = -\boldsymbol{\mu}_d \cdot \mathbf{B} \quad (14)$$

Given that

$$\begin{aligned} \boldsymbol{\mu}_d &= \mu_M \mathbf{S} \\ \mathbf{B} &= B_1 \cos(kz - \omega t + \phi) \hat{x} \end{aligned}$$

Substitute to get:

$$\begin{aligned} H_1 &= -\mu_M S_x B_1 \cos(kz - \omega t + \phi) \\ &= -\mu_M \frac{(S_+ + S_-)}{2} B_1 \frac{\exp(i(kz - \omega t + \phi)) + \exp(-i(kz - \omega t + \phi))}{2} \\ &= -\underbrace{\frac{\mu_M B_1}{4}}_{\hbar\Omega} (S_+ + S_-) (\exp(i(kz - \omega t + \phi)) + \exp(-i(kz - \omega t + \phi))) \\ &= \hbar\Omega (S_+ + S_-) (\exp(i(kz - \omega t + \phi)) + \exp(-i(kz - \omega t + \phi))) \end{aligned} \quad (15)$$

Throughout the calculations, we will neglect terms with fast oscillations (rotating-wave approximation, neglecting  $\exp(\pm i(\omega + \omega_0)t)$  or higher-freq terms). Also note that in some literature [5], the prefactor has a 1/2 which is due to a different definition of  $\hbar\Omega = \mu_M B_1 / 2$ .

The general wavefunction is entangled between the two degrees of freedom (internal and motional), and can be written as a superposition of product states (but its entirety is not necessarily a product state):

$$\Psi = \sum_{M_z=\downarrow,\uparrow} \sum_{n=0}^{\infty} C_{M_z,n}(t) |M_z\rangle |n\rangle \quad (16)$$

In the Heisenberg picture, considering the evolution of the hamiltonian  $H_1 \rightarrow H'_1 = U_0^\dagger(t) H_1 U_0(t)$ , where  $U_0(t) = \exp\left(-i\left(\frac{H_0}{\hbar}\right)t\right) = \exp(-i\omega_0 t)$ . Note also that  $kz = kz_0(ae^{-i\omega_z t} + a^\dagger e^{i\omega_z t})$ .

The Hamiltonian is hence calculated by:

$$H'_1 = \hbar\Omega (S_+ \exp(i\omega_0 t) + S_- \exp(-i\omega_0 t)) [\exp(i(kz - \delta t + \phi)) + \exp(-i(kz - \delta t + \phi))] \quad (17)$$

Simplifying to get:

$$H'_1 = \hbar\Omega S_+ \exp\left(i\left[\eta(ae^{-i\omega_z t} + a^\dagger e^{i\omega_z t}) - \delta t + \phi\right]\right) + \text{h.c.} \quad (17)$$

where  $\delta \equiv \omega - \omega_0$ , and  $\eta \equiv kz_0$  is the Lamb-Dicke parameter, characterizing the coupling strength between an ion's internal states and its motional states. For resonant transitions,  $\delta \simeq \omega_z(n' - n)$  where  $n'$  and  $n$  are integers.

### 2.3 Rabi Oscillation

The coefficients  $C_{\uparrow,n'}$  and  $C_{\downarrow,n}$  for  $\Psi$  can be solved effectively through simultaneous 1st-order (time-wise) differential equations (detail omitted), resulting in Rabi Oscillations between the states  $|\uparrow, n'\rangle$  and  $|\downarrow, n\rangle$ . The superposition state is defined as  $|\psi\rangle = C_{\downarrow,n} |\downarrow, n\rangle + C_{\uparrow,n'} |\uparrow, n'\rangle = [C_{\uparrow,n'}, C_{\downarrow,n}]^T$ , so considering just the time-evolution matrix entries of the resonant case:

$$\Psi(t) = \begin{bmatrix} \cos(\Omega_{n',n} t) & -ie^{i[\phi+\frac{\pi}{2}|n'-n|]} \sin(\Omega_{n',n} t) \\ -ie^{-i[\phi+\frac{\pi}{2}|n'-n|]} \sin(\Omega_{n',n} t) & \cos(\Omega_{n',n} t) \end{bmatrix} \Psi(0) \quad (18)$$

where the Rabi frequencies are given as

$$\Omega_{n',n} \equiv \Omega \left| \langle n' | e^{i\eta(a+a^\dagger)} | n \rangle \right| \quad (19)$$

A special case is when the Lamb-Dicke limit is satisfied, where the amplitude of the ion's motion in the direction of radiation is much less than  $\lambda/2\pi$ , or equivalently:

$$\langle \Psi_{motion} | k^2 z^2 | \Psi_{motion} \rangle^{1/2} \ll 1 \quad (20)$$

A less strict condition is where  $\eta \ll 1$  which is true if the Lamb-Dicke limit is satisfied, but the converse isn't guaranteed. When the Lamb-Dicke limit is satisfied, the Hamiltonian in (17) can be expanded to:

$$H'_1 \simeq \hbar\Omega S_+ (1 + i\eta(ae^{-i\omega_z t} + a^\dagger e^{i\omega_z t})) \exp(i(-\delta t + \phi)) + \text{h.c.} \quad (21)$$

There are three types of useful transitions: the carrier ( $n' = n, |g, n\rangle \rightarrow |e, n\rangle$ ), the first red sideband ( $n' = n-1, |g, n\rangle \rightarrow |e, n-1\rangle$ ), and the first blue sideband ( $n' = n+1, |g, n\rangle \rightarrow |e, n+1\rangle$ ) whose Rabi frequencies, in the Lamb-Dicke limit, are given by  $\Omega$ ,  $\eta\sqrt{n}\Omega$  and  $\eta\sqrt{n+1}\Omega$  respectively.

e.g. Take the case of red sideband where  $\delta = -\omega_z$  and  $\phi = -\frac{\pi}{2}$ , then equation (21) further simplifies:

$$\begin{aligned} H'_1 &\simeq \hbar\Omega S_+ (1 + i\eta(ae^{-i\omega_z t} + a^\dagger e^{i\omega_z t})) \exp(i(\omega_z t - \pi/2)) + \text{h.c.} \\ &\simeq \hbar\Omega S_+ i\eta a \exp(-i\pi/2) + \text{h.c.} \\ &\simeq \hbar\eta\Omega(S_+ a + S_- a^\dagger) \end{aligned} \quad (22)$$

This Hamiltonian is the same as the “Jaynes-Cummings Hamiltonian” in QED, describing the coupling of a two-level atom to a single mode of the (quantized) radiation field. Hence driving transitions between states will create entanglement between the internal and motional states, providing basis for two-qubit quantum logic gates.

For clarity, the Hamiltonians of the sidebands (red & blue) and the carrier cases could be expanded (in the Lamb-Dicke regime) in the following forms:

$$H_{rsb} \simeq \frac{\hbar\eta\Omega}{2} (\sigma_+ a e^{i\phi} + \sigma_- a^\dagger e^{-i\phi}) \quad (23)$$

$$H_{car} \simeq \frac{\hbar\eta\Omega}{2} (\sigma_+ e^{i\phi} + \sigma_- e^{-i\phi}) \quad (24)$$

$$H_{bsb} \simeq \frac{\hbar\eta\Omega}{2} (\sigma_+ a^\dagger e^{i\phi} + \sigma_- a e^{-i\phi}) \quad (25)$$

where  $S_{\pm} = \sigma_{\pm}/2$  and  $\omega_z = \nu$  is the harmonic oscillator frequency.

## 2.4 Open Quantum Systems

So far our discussion has been limited to assuming a closed quantum system which is an idealisation of real systems. In reality, we mostly only treat (sub)systems which interact with the environment. We thus unavoidably need a formulation of Open Quantum Theory which can deduce the equations of motion of the reduced systems from the total system (with environment).

The Lindblad Master Equation [10] describes the quantum dynamics of a subsystem of interest separated from the environment of the more complicated total system (the simplest case with only one relevant frequency considered).

$$\frac{d}{dt}\rho(t) = -i[H + H_{int}(t), \rho(t)] + \sum_n \left( L_n \rho(t) L_n^\dagger - \frac{1}{2} \{L_n^\dagger L_n, \rho(t)\} \right) \quad (26)$$

where the operators  $L_n$  are the jump operators associated with decoherence and noise from interaction with the environment,  $H$  and  $H_{int}(t)$  are the Hamiltonians of the subsystem (of interest) and the coupling (with the environment) respectively, and  $\rho(t)$  is the density operator describing the state of interest. Each  $n$  is associated with one channel of possible decoherence.

For numerical simulations, we model  $L_n = \sqrt{\gamma_n} A_n$  where  $A_n$  is the coupling (between the system and the environment) operator while  $\gamma_n$  is the corresponding rate.

Though formulated mathematically, it is still hard to solve a particular system with the Master equation by hand analytically. However, one can numerically solve a time-evolutionary problem in this way, such as tackling the standard Rabi oscillation discussed before, which certainly occurs experimentally under some (probably undesirable) interactions with the environment. It is worthwhile to note that even though calculations based on the traditional Schrödinger equation are usually more efficient, the Master equation should be applied for better accuracy when the coupling with environment is not negligible.

To see the effect of environment in influencing a physical system of interest, we demonstrate the phenomenon of decoherence using Qutip [11] package to solve the Lindblad master equation (modeled by time-evolving a Jaynes-Cummings Hamiltonian, coupled between the internal spin states and motional SHM states). Without decoherence, the probabilities of measuring spin-down (or up) would oscillate between 0 and 1 as a non-dissipative trigonometric function. However, decoherence (due to coupling with environment) leads to dissipation and a decaying trigonometric time-dependence, as in *Figure 6*. The skewing tendency is due to parameters representing qubit relaxation (i.e. turning  $|0\rangle \rightarrow |1\rangle$ ).

## 2.5 Stimulated Raman Transitions

A schematic setup is shown in *Figure 7*. The relevant Hamiltonian, replaced from (15), is given by:

$$H_1 = \hbar\Omega(S_+ + S_-)(\exp(i[(\mathbf{k}_1 - \mathbf{k}_2) \cdot \mathbf{x} - (\omega_{L1} - \omega_{L2})t + \phi]) + \text{h.c.}) \quad (27)$$

The transition is driven between state  $|\uparrow\rangle$  and  $|\downarrow\rangle$  through another state  $|3\rangle$  by stimulated-Raman transitions using plane EM waves (typically considering electric dipole transitions). It is possible

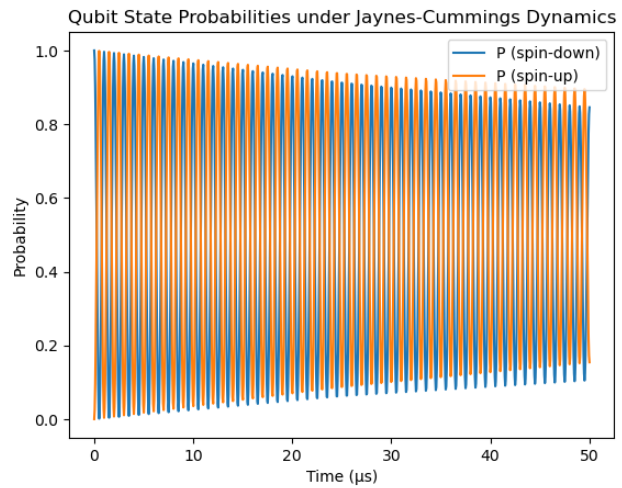


Figure 6: Effects of Decoherence: Loss of Quantum Information

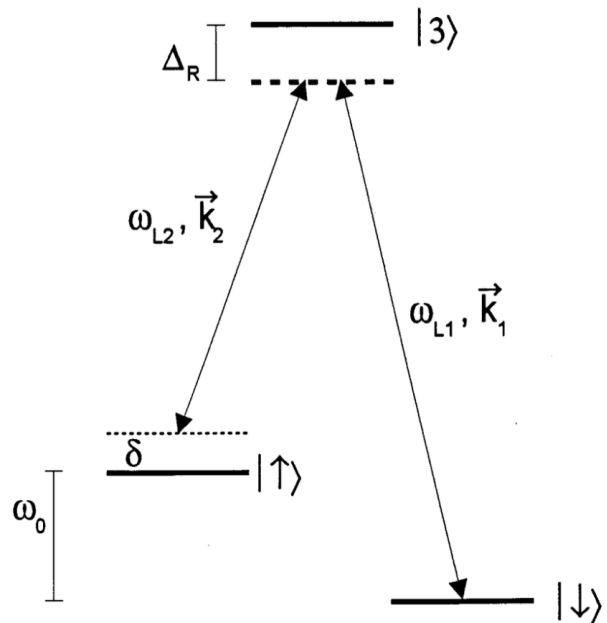


Figure 7: Stimulated-Raman Transitions

to calculate theoretically the wavefunctions in the Schrödinger picture as well as calculating the matrix elements through a set of simultaneous 1st-order differential equations. An optical Stark shift should also be included, but may be neglected if the shifts are made equal for  $|\uparrow\rangle$  and  $|\downarrow\rangle$  since no additional phase shifts caused.

The mathematics involved would be the same as for a two-level system if one makes the difference between wavevectors/relative phases approximately equal to the wavevector/relative phase discussed before in the original Hamiltonian (15).

## 2.6 Initialisation (Cooling Techniques)

For preparation of ions in the ground state ( $|n = 0\rangle$  motional state) in initialisation. A combination of Doppler cooling and sideband laser cooling is used.

Doppler cooling is achieved in the following way: an atom moving toward a laser beam has transition frequencies which are slightly higher in energy than an atom moving away. If the laser is tuned (red-detuned) such that it is absorbed only by approaching atoms, then the atoms slow down (lose momentum) because the photons kick them in the opposite direction (for emission it is roughly isotropic so the net effect is determined by just the absorption preference). Doppler cooling usually only cools to a temperature of about 1 mK (Doppler cooling limit), so sideband cooling is necessary.

The basic idea of sideband cooling is very simple: a laser is used to excite atoms which are in any state other than the desired initial state into some high-energy state, and combined with random relaxation processes this leads to preferential population of the desired state. [3]

In the schematic diagram *Figure 8*, the cooling process is achieved by the following sequence:  $|\downarrow\rangle|n\rangle \xrightarrow{a} |\uparrow\rangle|n-1\rangle \xrightarrow{b} |\downarrow\rangle|n-1\rangle$ . Part (a) is induced by a stimulated-Raman transition tuned to the first red sideband. In part (b), a third laser pumps the state to the higher auxiliary state which then spontaneously decays and partially results in a spin-down lower motional state (this is highly efficient even if sometimes it pumps back to the spin-up state originally). The process is then repeated until we reduce to the ground state.

This only shows the traditional laser-based manipulations for logic gate controls. However, microwave or electronically-based techniques are also possible to realise quantum logic gate operations, albeit facing a key challenge in individual addressing (discussed in the following section). Moreover, another useful method applied widely is the EIT cooling [12] which involves a 3-level system. The detail is rather involved, but the key is that the detuning is chosen such that the atomic system is pumped to a dark state not coupled to the laser fields, thus significantly decreasing the rate of spontaneous emissions (hence intrinsic heating processes). The general advantage is thus that EIT cooling substantially shortens the cooling time to reach ground states over a range of oscillation frequencies compared to sideband cooling. It also relies on a more robust cooling technique with a smaller number of optimization parameters.

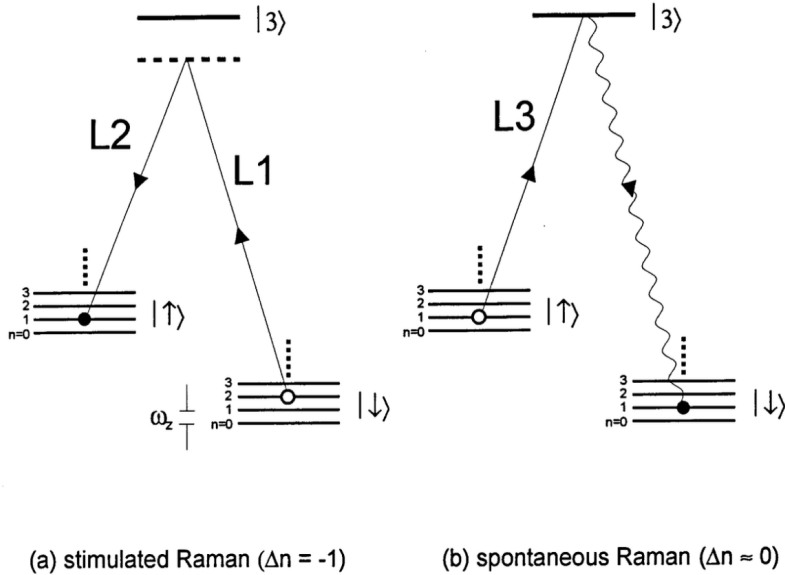


Figure 8: Sideband Laser Cooling

## 2.7 Quantum Logic Gates

Single-bit rotations can be characterized by the following unitary operator:

$$R(\theta, \phi) = \begin{bmatrix} \cos(\theta/2) & -ie^{i\phi} \sin(\theta/2) \\ -ie^{-i\phi} \sin(\theta/2) & \cos(\theta/2) \end{bmatrix} \quad (28)$$

Where we have started from the transformation of (18), setting  $n' = n$  and  $\theta = 2\Omega_{n',n}t$ . This is equivalent to applying an oscillating magnetic field in the  $x$  direction for the spin-1/2 model. From different parameter choices we can obtain the desired single-qubit unitary gates such as the standard Pauli gates, Hadamard, etc.

For universal computing it is also necessary to consider the implementation of 2-qubit entangling gates (i.e. CNOT or CZ gates). This can be implemented by the Cirac-Zoller CZ scheme [8], or using the more advanced Mølmer-Sørensen (MS) gate [9].

The Cirac-Zoller scheme utilises the standard coupling of the internal energy levels of the  $n$ -th ion ( $|g\rangle_n, |e_0\rangle_n, |e_1\rangle_n, \dots$ ), the CM motional modes ( $|0\rangle, |1\rangle, \dots$ ) shared by all ions. Manipulations using red-sideband lasers are described by the Hamiltonian as in (22). Considering the interaction between  $|g\rangle_n$  and  $|e_q\rangle_n$  (where  $n$  specifies the selected ion and  $q$  is the polarization number), since  $S_+ = \sigma_+/2 = |e_q\rangle_n \langle g|/2$  and  $S_- = |g\rangle_n \langle e_q|/2$ , the Hamiltonian can be written as:

$$H_{n,q} = \frac{\hbar\eta\Omega}{2} (|e_q\rangle_n \langle g| a + |g\rangle_n \langle e_q| a^\dagger) \quad (29)$$

(where we have neglected the prefactor  $1/\sqrt{N}$  which is irrelevant for the core physics here)

To proceed, we may write the unitary operator  $U = \exp(-iHt/\hbar)$  with the time focused by laser beam chosen as  $t = k\pi/(\Omega\eta)$  (i.e.  $k\pi$  pulse):

$$U_n^{k,q} = \exp \left[ -ik\frac{\pi}{2} (|e_q\rangle_n \langle g| a + |g\rangle_n \langle e_q| a^\dagger) \right] \quad (30)$$

To actually implement the Cirac-Zoller CZ gate, we choose the control qubit to be the  $m$ -th ion, while the target qubit to be the  $n$ -th ion, both interacted with the CM motional modes  $|0\rangle, |1\rangle, \dots$  and initialised at the ground motional state  $|0\rangle$  (which is actually a rather strict condition requiring very low temperatures and avoided by the Mølmer-Sørensen gate). To illustrate the calculations, the following results can be very helpful:

$$\begin{aligned} U_n^{1,0} |g\rangle_n |0\rangle &= \exp(0) |g\rangle_n |0\rangle = |g\rangle_n |0\rangle \\ U_n^{1,0} |g\rangle_n |1\rangle &= -i \sin(\pi/2) (\langle e_0 \rangle_n \langle g|g \rangle) (a|1\rangle) = -i |e_0\rangle_n |0\rangle \\ U_n^{1,0} |e_0\rangle_n |0\rangle &= -i \sin(\pi/2) (\langle g\rangle_n \langle e_0|e_0 \rangle) (a^\dagger |0\rangle) = -i |g\rangle_n |1\rangle \\ U_n^{2,1} |g\rangle_n |0\rangle &= \exp(0) |g\rangle_n |0\rangle = |g\rangle_n |0\rangle \\ U_n^{2,1} |g\rangle_n |1\rangle &= \cos(\pi) |g\rangle_n |1\rangle = -|g\rangle_n |1\rangle \\ U_n^{2,1} |e_0\rangle_n |0\rangle &= \exp(0) |e_0\rangle_n |0\rangle = |e_0\rangle_n |0\rangle \\ U_n^{2,1} |e_0\rangle_n |1\rangle &= \exp(0) |e_0\rangle_n |1\rangle = |e_0\rangle_n |1\rangle \end{aligned}$$

Thus, if we apply unitary evolutions in the order of  $U_m^{1,0} U_n^{2,1} U_m^{1,0}$  on the possible initialised states, the CZ gate can be constructed as:

$$C_Z = U_m^{1,0} U_n^{2,1} U_m^{1,0} = \begin{pmatrix} 1 & 0 & 0 & 0 \\ 0 & 1 & 0 & 0 \\ 0 & 0 & 1 & 0 \\ 0 & 0 & 0 & -1 \end{pmatrix} \quad (31)$$

where the basis for this matrix is  $\{|g\rangle_m |g\rangle_n |0\rangle, |g\rangle_m |e_0\rangle_n |0\rangle, |e_0\rangle_m |g\rangle_n |0\rangle, |e_0\rangle_m |e_0\rangle_n |0\rangle\}$ , and the entries can be verified easily.

Trivially, it followed that applying  $HC_ZH$  is equivalent to a standard CNOT entangling gate. In fact, any non-trivial entangling two-qubit gate (in combination with single-qubit gates) would suffice for universal computation.

As characterised by the calculations, the Cirac-Zoller scheme requires two strict conditions: (i) individual addressing of a particular pair of ions. (ii) very low temperature to ensure the motional state is initialised at  $|0\rangle$ . These can be very unpractical, so an improved method for 2-qubit entangling gate, the Mølmer-Sørensen gate, is more useful currently.

The Mølmer-Sørensen scheme is outlined in *Figure 9*. For two ions chosen, lasers are used to couple the states  $|ggn\rangle \leftrightarrow \{|egn+1\rangle, |gen-1\rangle\} \leftrightarrow |een\rangle$ , through a combination of red or blue sidebands. However, the lasers are particularly detuned from the sidebands such that no populations can be gained in the intermediate states  $\{|egn+1\rangle, |gen-1\rangle\}$  as they are kept off-resonant.

It is mathematically possible to show, via standard second-order perturbation theory, by restricting the intermediate states considered to  $\{|egn+1\rangle, |gen-1\rangle\}$ , that the equivalent frequency of oscillations  $\tilde{\Omega}$  between states  $|gg\rangle$  and  $|ee\rangle$  is given by:

$$\tilde{\Omega} = -\frac{(\Omega\eta)^2}{2(\nu - \delta)} \quad (32)$$

where  $\delta = \omega_1 - \omega_{eg}$  is the small detuning of the laser, assuming both ions with the same Lamb-Dicke parameter  $\eta$  and Rabi frequency  $\Omega$ .

The fundamental importance of (32) is the independence of  $n$  (mathematically due to a difference of two terms with factor  $n + 1$  and  $n$  respectively), which means the evolution of internal states of the ions is insensitive to the vibrational quantum numbers, so any mixture of superposition of vibrational states (phonon number) is allowed for this interaction. Additionally, this does not limit to the pair of  $\{|gg\rangle, |ee\rangle\}$ , as  $\{|ge\rangle, |eg\rangle\}$  can also be entangled by the same mechanics.

In practice, one applies laser detuned with  $\pm\delta$  to both ions continuously, so there will be two more paths in addition to the two paths outlined in *Figure 9*. The physics is only changed by multiplying (32) by a factor of 2. The unitary evolution operator for the two-ion states can be described by the following:

$$\begin{aligned} |gg\rangle &\rightarrow \cos\left(\frac{\tilde{\Omega}T}{2}\right)|gg\rangle + i \sin\left(\frac{\tilde{\Omega}T}{2}\right)|ee\rangle \\ |ee\rangle &\rightarrow \cos\left(\frac{\tilde{\Omega}T}{2}\right)|ee\rangle + i \sin\left(\frac{\tilde{\Omega}T}{2}\right)|gg\rangle \\ |ge\rangle &\rightarrow \cos\left(\frac{\tilde{\Omega}T}{2}\right)|ge\rangle - i \sin\left(\frac{\tilde{\Omega}T}{2}\right)|eg\rangle \\ |eg\rangle &\rightarrow \cos\left(\frac{\tilde{\Omega}T}{2}\right)|eg\rangle - i \sin\left(\frac{\tilde{\Omega}T}{2}\right)|ge\rangle \end{aligned}$$

This is sufficient for a non-trivial entangling gate. For example, setting  $\tilde{\Omega}T/2 = \pi/4$ , one reads  $|gg\rangle \rightarrow \frac{1}{\sqrt{2}}(|gg\rangle + i|ee\rangle)$ , which is a maximally-entangled state evolved from a product state  $|gg\rangle$ .

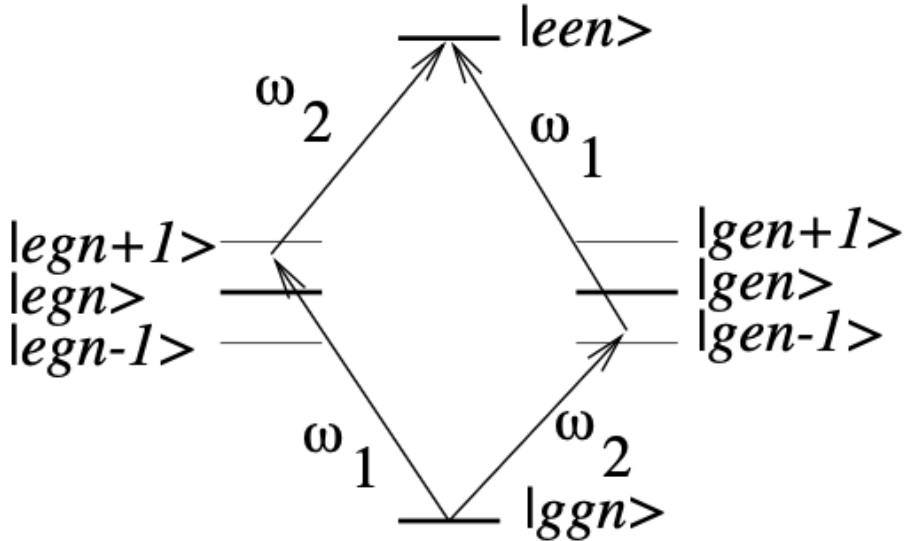


Figure 9: Laser Detuning for MS Gate [9]

## 2.8 Detection of Internal States

As with all quantum mechanical states, the unitary evolution of states contains quantum information which is valuable but nonetheless obscure to an observer. For physical implementation we also need a scheme for measurement which accurately returns the eigenstate of the measured outcome.

This is not hard to achieve with lasers: we may tune the beam to specifically trigger a stimulated transition with a third state (which quickly decays back to  $|0\rangle$ , say), leading to detectable fluorescence. But there will not be no scattered photons to the other state (i.e.  $|1\rangle$ ). Hence if we detect for a sufficient amount of photons it will be possible to ensure accurate measurement of state ( $|0\rangle$  or  $|1\rangle$ ), as well as the corresponding probability (amplitude norm squared) if the state is in a general superposition in this basis.

## 3 Dynamical Decoupling (MW) [2]

It is generally preferable to use lasers over microwaves for manipulations of trapped ions due to easier addressing of individual ions as well as greater field gradients due to the smallness of  $\lambda$ . However, microwave technology is more cost-efficient, scalable while maintaining high fidelity. One of the biggest issues in individual ion addressing can be solved by dynamical decoupling.

### 3.1 Theory

The key use of dynamical decoupling is to suppress (or reinforce, if desired) the effect of the state-dependent displacement (SDD), or the interaction which drives two-qubit gates.

The Hamiltonian describing the SDF is described as: [4]

$$\hat{H} = \frac{\hbar\Omega}{2}e^{-i(\omega-\omega_q)t}\hat{\sigma}_+(e^{i\phi_{\text{field}}} + \eta e^{i\phi_{\text{grad}}}(e^{-i\omega_m t}\hat{a} + e^{i\omega_m t}\hat{a}^\dagger)) + \text{h.c.} \quad (33)$$

Where  $\omega$ ,  $\omega_q$  and  $\omega_m$  are the frequencies of the microwave field, qubit transition and ion motion respectively and  $\hat{\sigma}_+ = |1\rangle\langle 0|$  acts on the qubit states.  $\phi_{\text{field}}$  and  $\phi_{\text{grad}}$  are the phases of the field  $B_x$  and its partial derivative respectively.  $\Omega$  is the Rabi-frequency and  $\eta$  is the Lamb-Dicke parameter.

We consider the three cases:  $\omega = \omega_q$  (driven in resonance),  $\omega = \omega_q - (\omega_m + \delta)$  (red motional sideband) and  $\omega = \omega_q + (\omega_m + \delta)$  (blue motional sideband). For the first case:

$$\hat{H}_{\text{DD}} \simeq \frac{\hbar\Omega}{2}\hat{\sigma}_+e^{i\phi_{\text{field}}} + \text{h.c.} = \frac{\hbar\Omega_{\text{DD}}}{2}e^{i\phi_{\text{DD}}}\hat{\sigma}_+ + \text{h.c.} \quad (34)$$

Where we have neglected the motional coupling since  $\eta\Omega \ll \omega_m$  assumed. We label this as the DD (dynamical decoupling) case.

For the red sideband case:

$$\begin{aligned} \hat{H}_{\text{red}} &= \frac{\hbar\Omega}{2}e^{i(\omega_m+\delta)t}\hat{\sigma}_+(e^{i\phi_{\text{field}}} + \eta e^{i\phi_{\text{grad}}}(e^{-i\omega_m t}\hat{a} + e^{i\omega_m t}\hat{a}^\dagger)) + \text{h.c.} \\ &= e^{i\phi_{\text{grad}}}\left[\frac{\hbar\Omega}{2}e^{i(\phi_{\text{field}}-\phi_{\text{grad}})}\hat{\sigma}_+e^{i(\omega_m+\delta)t} + \frac{\hbar\eta\Omega}{2}\hat{\sigma}_+(e^{i\delta t}\hat{a} + \underbrace{e^{i2\omega_m t}e^{i\delta t}\hat{a}^\dagger}_{>0})\right] + \text{h.c.} \end{aligned} \quad (35)$$

(the third term neglected due to rotating-wave approximation)

For the blue sideband, similarly:

$$\hat{H}_{\text{blue}} = e^{i\phi_{\text{grad}}} \left[ \frac{\hbar\Omega}{2} e^{i(\phi_{\text{field}} - \phi_{\text{grad}})} \hat{\sigma}_+ e^{-i(\omega_m + \delta)t} + \frac{\hbar\eta\Omega}{2} \hat{\sigma}_+ (e^{-i\delta t} \hat{a}^\dagger + \underbrace{e^{-i2\omega_m t} e^{-i\delta t} \hat{a}}_{->0}) \right] + \text{h.c.} \quad (36)$$

Combining the two sideband cases, we may write the Hamiltonian as a sum of contributions from state-dependent force and off-resonant carrier driving: (we neglect the overall phase factor  $e^{i\phi_{\text{grad}}}$  since it is non-physical)

$$\hat{H}_{\text{SB}} = \hat{H}_{\text{off}} + \hat{H}_{\text{SDF}} \quad (37)$$

where

$$\hat{H}_{\text{SDF}} = \frac{\hbar\eta\Omega}{2} \hat{\sigma}_+ (e^{i\delta t} \hat{a} + e^{-i\delta t} \hat{a}^\dagger) + \text{h.c.} \quad (38)$$

$$\hat{H}_{\text{off}} = \frac{\hbar\Omega}{2} e^{i(\phi_{\text{field}} - \phi_{\text{grad}})} \hat{\sigma}_+ (e^{i(\omega_m + \delta)t} + e^{-i(\omega_m + \delta)t}) + \text{h.c.} \quad (39)$$

Using the condition  $\Omega_{\text{SB}} = \eta\Omega$  and  $\delta = 0$ , we may further simplify  $\hat{H}_{\text{SDF}}$ . ( $\hat{H}_{\text{off}}$  can be trivially simplified into a cosine wave too)

$$\hat{H}_{\text{SDF}} = \frac{\hbar\Omega_{\text{SB}}}{2} (\hat{\sigma}_+ + \hat{\sigma}_-) (\hat{a} + \hat{a}^\dagger) = \frac{\hbar\Omega_{\text{SB}}}{2} \hat{\sigma}_x (\hat{a} + \hat{a}^\dagger) \quad (40)$$

It is possible to write  $\sigma_x = |+\rangle\langle+| - |-\rangle\langle-|$ , so a change of basis gives:

$$\hat{H}_{\text{SDF}} = \frac{\hbar\Omega_{\text{SB}}}{2} |+\rangle\langle+| (\hat{a} + \hat{a}^\dagger) - \frac{\hbar\Omega_{\text{SB}}}{2} |-\rangle\langle-| (\hat{a} + \hat{a}^\dagger) \quad (41)$$

Hence it is obvious that the force experienced is positive if the qubit is in  $|+\rangle$  state and is negative if the qubit is in  $|-\rangle$ .

Consider the Hamiltonian (34) when  $\phi_{\text{DD}} = k\pi$ , then:

$$\hat{H}_{\text{DD}} = \pm \frac{\hbar\Omega_{\text{DD}}}{2} (\hat{\sigma}_+ + \hat{\sigma}_-) = \pm \frac{\hbar\Omega_{\text{DD}}}{2} \hat{\sigma}_x \quad (42)$$

Now in this case both  $\hat{H}_{\text{DD}}$  and  $\hat{H}_{\text{SDF}}$  are proportional to  $\hat{\sigma}_x$ , so it follows  $[\hat{H}_{\text{DD}}, \hat{H}_{\text{SDF}}] = 0$ , and there is no change for SDF dynamics. If instead the phase is  $\phi_{\text{DD}} = \pi/2 + k\pi$  (in-quadrature case), then given  $\Omega_{\text{DD}} \gg \Omega_{\text{SB}}$ , the DD tone rapidly drives Rabi oscillations between the states  $|+\rangle$  and  $|-\rangle$ . Such rapid change in SDF directions (depending on the basis ket) will effectively suppress any amplitude of motion gained due to SDF and allow individual addressing.

### 3.2 Experimental Design and Demonstration

A first test of the above idea is demonstrated by *Figure 10*. To inhibit motional entanglement, a dynamical decoupling tone drives the qubit with a variable phase (relative to the average phase of the two sidebands).  $P|0\rangle$  is measured for a fixed pulse duration (red star), such that suppression of the state-dependent displacement corresponds to  $P|0\rangle > 0.6$ . The SDF is unaffected ( $P|0\rangle \approx 0.6$ ) or suppressed ( $P|0\rangle \approx 1$ ) for  $\phi_{\text{DD}} = 0$  and  $\phi_{\text{DD}} = \pi/2$  respectively. This demonstrates uses  $\Omega_{\text{DD}} \approx 60\Omega_{\text{SB}}$  to drive the ions.

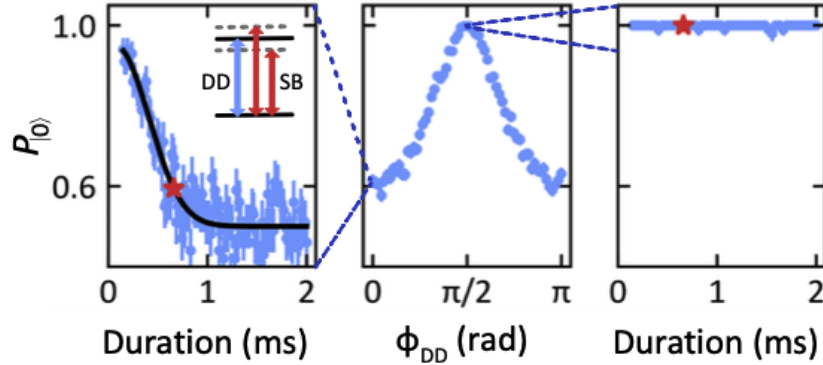


Figure 10: Phase-Controlled SDF Suppression

The crucial takeaway is that the phase between the DD driving and SDF at different spatial locations must vary in phase to address individual ions. A system proposed<sup>[2]</sup> is based on the microwave electrode geometry shown in *Figure 11*. Here we note that the magnetic field gradient is used to generate the SDF enabling entanglement, while the phase of the field gradient remains constant (SDF is phase-independent). The phase of the field, however, varies in positions (with respect to  $x$ ) and can be used to obtain suppression of the SDF (in phase at the field min at center while approximately at  $\pi/2$  away from it).

The process and results are illustrated by *Figure 12*. Diagram (a) demonstrates the variation of the phase of the microwave and its gradient (fitted) with the ion position. (b) clearly shows two zones created: a memory zone where SDF is suppressed and an interaction zone where it is not, showing effective spatial control of SDF.

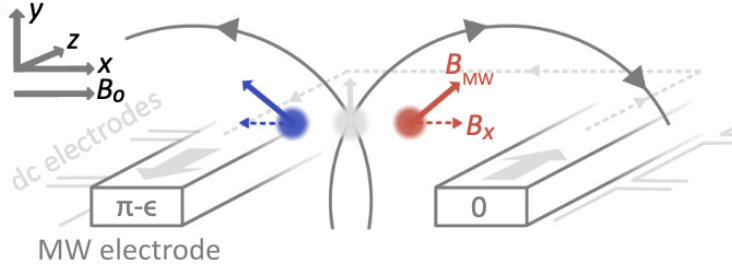


Figure 11: Basic Surface-Trap Design (Microwave-based)

### 3.3 Magnetic Field Modeling

To clearly validate the idea of last section, we take a quantitative approach to calculate the magnetic field strength  $\mathbf{B}$  due to the opposing electrodes in *Figure 11* from Ampere's Law:

$$\oint \mathbf{B} \cdot d\ell = \mu_0 I_{\text{enc}} \quad (43)$$

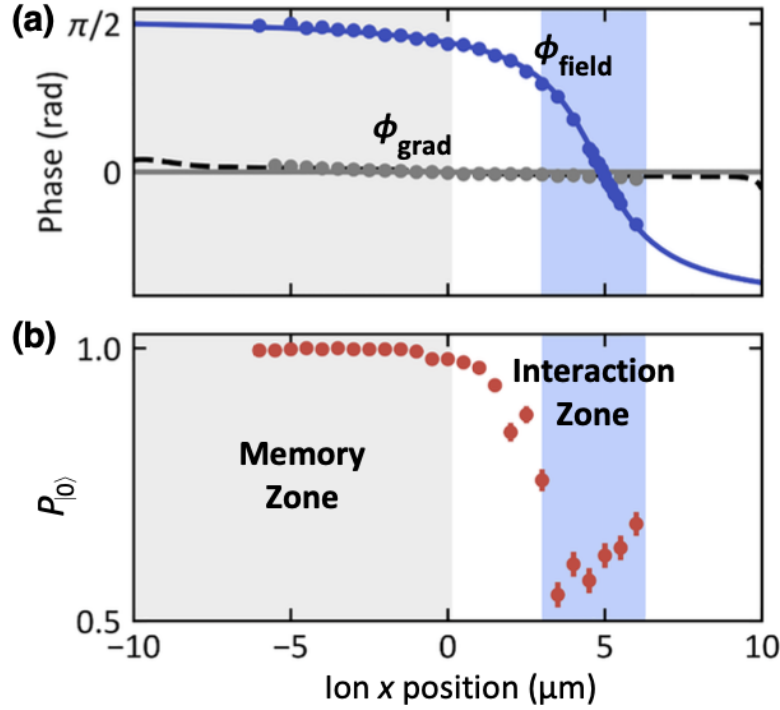


Figure 12: Spatially Selective Ion-Motion Interaction

Because generally the width of the electrodes is much smaller than the displacement of the point in space from the electrodes, we may treat this surface current as a line current flowing without dimension, in calculations. (In fact, they are approximately equivalent for  $K = I_0/\ell$  where  $K$  is the magnitude of the surface current density,  $I_0$  is the magnitude of the current (proper) and  $\ell$  is the width of the electrode surface.)

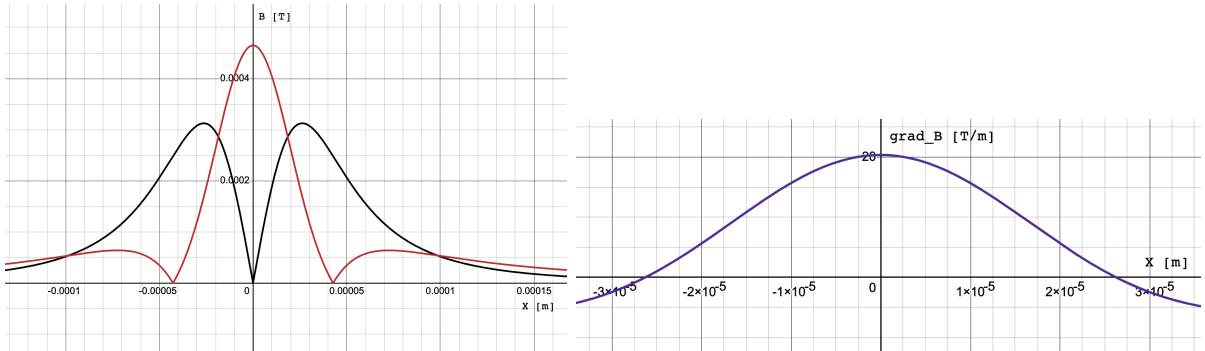


Figure 13: Plots of analytic solutions: (left)  $B$ -components & (right)  $B_x$ -gradient (all at  $y = 40\mu\text{m}$ )

From the basic law of magnetostatics in (43) and some elementary geometric considerations, we may write down the Cartesian components of the net magnetic field strength  $B_x$  and  $B_y$  (see the axes defined by *Figure 11*) due to the two electrodes (in the region between the two electrodes),

assuming superposition of magnetic field strength. The parallel (to plane) component is given by:

$$B_x(x, y) = \frac{\mu_0 I_0 y}{2\pi} \cos(\omega t + \phi) \left( -\frac{1}{(x+d)^2 + y^2} + \frac{1}{(x-d)^2 + y^2} \right) \quad (44)$$

where  $I_0$  ( $\simeq 0.141A$ ) is the magnitude of current for each electrode,  $\omega$  is the AC frequency of the current (with an arbitrary phase  $\phi$  which is irrelevant), and  $d$  is the distance between the centre of each electrode and the origin of the system where  $B_x = 0$ .

The perpendicular (to plane) component is given as:

$$B_y(x, y) = \frac{\mu_0 I_0}{2\pi} \cos(\omega t + \phi) \left( \frac{x+d}{(x+d)^2 + y^2} + \frac{d-x}{(x-d)^2 + y^2} \right) \quad (45)$$

*Figure 13*, drawn by Desmos, shows the above analytic solutions at  $y = 40\mu m$ . The left diagram shows the black plot  $|B_x|$  and the red plot  $|B_y|$ . It can be clearly observed from the pattern that the central location  $x = 0$  has a zero  $B_x$  whilst a maximum  $B_y$  as expected, due to destructive interference of  $B_x$  and constructive interference of  $B_y$ . The right diagram, on the other hand, shows the value of  $\frac{\partial B}{\partial x}$ , which is approximately uniform and positive for small deviation from the center.

The electrodes model in *Figure 11* is simulated using Comsol Multiphysics numerically to compare with the analytic solution from Ampere's law, producing *Figure 14*. The two diagrams above are 2D plots for  $|B_x|$  and  $|B_y|$  respectively, while the two lower are 1D plots for those at  $y = 40\mu m$ .

Confirming that our model is correct, the key takeaway is that the phase of  $B_x$ -gradient (responsible for SDF) does not change with position. However, the phase of the field  $B_x$  varies with spatial location, as the field switches from being dominated by one electrode to the other, as the trapped ion is moved in the region between the electrodes. This change in phase of  $B_x$  is what physically could be implemented to obtain suppression of SDD, as outlined from last section.

### 3.4 Alternative Design

A different trap design is shown in *Figure 15*, where the chain of ions is now perpendicular to the microwave electrodes. This could be accomplished by using a multilayer surface trap, where buried microwave electrodes emerge under the ions. Here the additional interaction zone is enabled by a third microwave electrode creating a second DD phase flip (at a different position to the first). The three electrodes are assumed to be fed by independent microwave currents, where the central MW current is close to  $\pi$  radians out of phase with the other two.

One can utilise this design by setting the amplitudes of the DD currents through each electrode to control the positions of the selected ions (blue ones in *Figure 15*) and the interaction zone.

We demonstrate this idea concisely using a demo by Comsol Multiphysics [7] again. Here in *Figure 16* the magnetic field strength (absolute value) in the parallel ( $x$ ) direction of the ion chain is shown.

The parameters of the setup in *Figure 16* are as followed: The two electrodes are spaced centre-to-centre by  $40\mu m$  as in *Figure 15*, with an electrode-width ( $x$ -direction) of  $5\mu m$ . For simplicity this model only considers the DD drive in an arbitrary moment of time, with surface current in proportion of -1, 0.3, -0.125 respectively, counting from the leftmost electrode. The left figure shows a 2D plot of  $B_x$  generally over the space between the electrodes, while the right

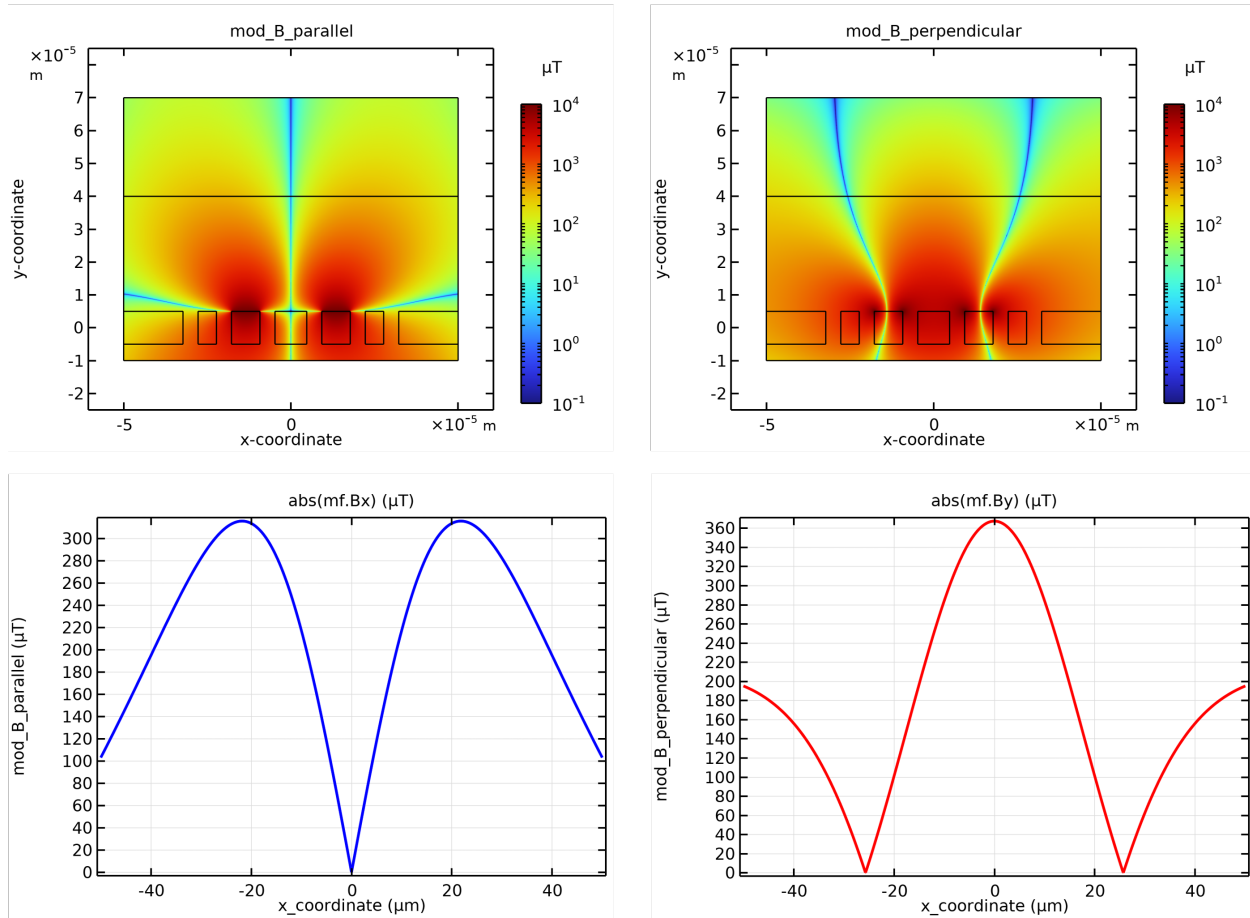


Figure 14: Numerically simulated model for spatial variations of  $|B_x|$  and  $|B_y|$  (matching the result in the literature<sup>[6]</sup>)

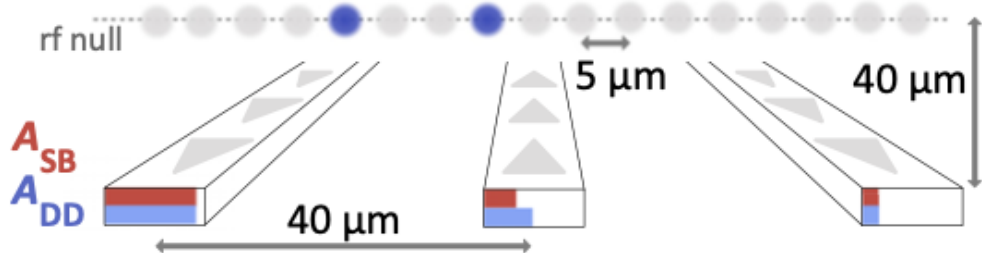


Figure 15: Design of Three Microwave Electrodes

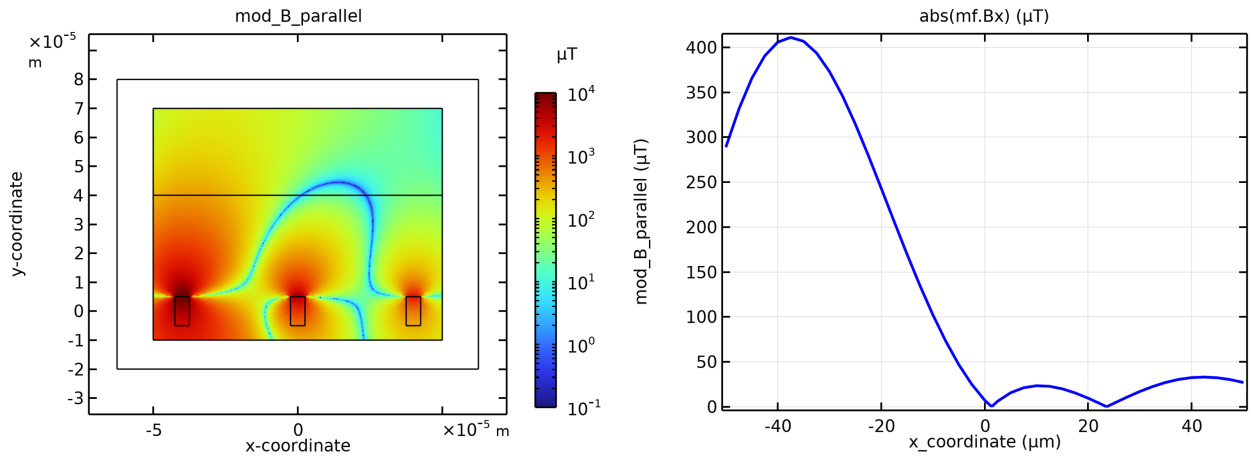


Figure 16: Magnetic Field ( $x$ -component) Modeled for a Three-Electrode Design

figure clearly shows the 1D variation at the height of  $y = 40\mu\text{m}$  where the chain of ions is located. We clearly observe two zeros at  $x \simeq 1.43\mu\text{m}$  and  $x \simeq 23.57\mu\text{m}$  respectively. Here is the position where the phases are shifted the most and can be considered as creating the interaction zones illustrated by the idea of *Figure 12* for addressing of desired ion(s). Certainly this modeling is only an approximate simulation which neglects a lot of technical detail and rooms of improvement, but still sufficient to illustrate the general picture.

## 4 Relevant Sources

- [1] Wineland, D. J., Monroe, C., Itano, W. M., Leibfried, D., King, B. E., & Meekhof, D. M. (1998). Experimental issues in coherent quantum-state manipulation of trapped atomic ions. *Journal of research of the National Institute of Standards and Technology*, 103(3), 259.
- [2] Smith, M. C., Leu, A. D., Gely, M. F., & Lucas, D. M. (2024). Individually Addressed Quantum Gate Interactions Using Dynamical Decoupling. *PRX Quantum*, 5(3), 030321.
- [3] Jones, J. A., & Jaksch, D. (2012). *Quantum Information, Computation and Communication*. Cambridge: Cambridge University Press.
- [4] Ospelkaus, C., Langer, C. E., Amini, J. M., Brown, K. R., Leibfried, D., & Wineland, D. J. (2008). Trapped-ion quantum logic gates based on oscillating magnetic fields. *Physical review letters*, 101(9), 090502.
- [5] Nielsen, M. A., & Chuang, I. L. (2010). *Quantum computation and quantum information*. Cambridge university press.
- [6] Weber, M. A., Löschner, C., Wolf, J., Gely, M. F., Hanley, R. K., Goodwin, J. F., ... & Lucas, D. M. (2023). Cryogenic ion trap system for high-fidelity near-field microwave-driven quantum logic. *Quantum Science and Technology*, 9(1), 015007.
- [7] COMSOL Inc. COMSOL Multiphysics®. v. 6.2.
- [8] Cirac, J. I., & Zoller, P. (1995). Quantum computations with cold trapped ions. *Physical Review Letters*, 74(20), 4091–4094.
- [9] Sørensen, A., & Mølmer, K. (1999). Quantum computation with ions in thermal motion. *Physical Review Letters*, 82(9), 1971–1974.
- [10] Manzano, D. (2020). A short introduction to the Lindblad master equation. *Aip advances*, 10(2).

- [11] Lambert, N., Giguère, E., Menczel, P., Li, B., Hopf, P., Suárez, G., Gali, M., Lishman, J., Gad hví, R., Agarwal, R., Galicia, A., Shammah, N., Nation, P., Johansson, J. R., Ahmed, S., Cross, S., Pitchford, A., & Nori, F. (2024). QuTiP 5: The Quantum Toolbox in Python. arXiv.
- [12] Lechner, R., Maier, C., Hempel, C., Jurcevic, P., Lanyon, B. P., Monz, T., ... & Roos, C. F. (2016). Electromagnetically-induced-transparency ground-state cooling of long ion strings. Physical Review A, 93(5), 053401.
- [13] Foot, C. J. (2005). Atomic physics (Vol. 7). Oxford university press.